nature communications

Article

https://doi.org/10.1038/s41467-024-47148-0

Synergistically optimized electron and phonon transport in high-performance copper sulfides thermoelectric materials via one-pot modulation

Received: 24 November 2023

Accepted: 21 March 2024

Published online: 28 March 2024

Check for updates

Yi-Xin Zhang[1], Qin-Yuan Huang[1], Xi Yan[1], Chong-Yu Wang[1], Tian-Yu Yang[1], Zi-Yuan Wang[1], Yong-Cai Shi[1], Quan Shan[1], Jing Feng[1] & Zhen-Hua Ge[1]

Optimizing thermoelectric conversion efficiency requires the compromise of electrical and thermal properties of materials, which are hard to simultaneously improve due to the strong coupling of carrier and phonon transport. Herein, a one-pot approach realizing simultaneous second phase and Cu vacancies modulation is proposed, which is effective in synergistically optimizing thermoelectric performance in copper sulfides. Multiple lattice defects, including nanoprecipitates, dislocations, and nanopores are produced by adding a refined ratio of Sn and Se. Phonon transport is significantly suppressed by multiple mechanisms. An ultralow lattice thermal conductivity is therefore obtained. Furthermore, extra Se is added in the copper sulfide for optimizing electrical transport properties by inducing generating Cu vacancies. Ultimately, an excellent figure of merit of ~1.6 at 873 K is realized in the $Cu_{1.992}SSe_{0.016}(Cu_2SnSe_4)_{0.004}$ bulk sample. The simple strategy of inducing compositional and structural modulation for improving thermoelectric parameters promotes low-cost high-performance copper sulfides as alternatives in thermoelectric applications.

Thermoelectric (TE) conversion technology is capable of realizing power generation and small refrigeration[1–3]. The excellent conversion efficiency of the thermoelectric materials that are the key component of TE devices is the main parameter by which to evaluate the potential candidates[4–6]. Other requirements, including service stability, mechanical performance, cost, and toxicity, are essential to promote thermoelectric materials in device assembly and extensive application[7]. The conversion efficiency is gauged by the thermoelectric dimensionless figure of merit: $ZT = S^2\sigma T/\kappa$, where S, σ, T and κ are the Seebeck coefficient, electrical conductivity, absolute temperature and total thermal conductivity, respectively[8]. It is difficult to simultaneously optimize the electrical and thermal transport properties because of the complex coupling of various TE parameters[9,10]. Introducing a second phase by in situ precipitates[11,12,13] or phase separation[14,15] has been proven to be effective in restraining the lattice thermal conductivity, which can be individually improved. Decoupling other TE parameters usually involves complex and multistep optimization strategies[16,17]. In addition, the service stability of thermoelectric materials must be considered, which requires the maintenance of the composition and microstructure of TE materials under external temperature or an electrical field.

Copper sulfides have been studied in the TE field for more than 190 years, which possess ultralow lattice thermal conductivity because of the strong phonon scattering effects and the vanished transverse wave phonon vibration caused by disordered Cu ion migration[18]. Lots of efforts have been put to improve the electrical transport properties while maintaining the low thermal conductivity of copper sulfides. The typical strategies are composition off-stoichiometry[19,20], element-

[1]Faculty of Materials Science and Engineering, Kunming University of Science and Technology, Kunming 650093, China. e-mail: zge@kust.edu.cn

doping[21–25] and second phase compositing[26–28]. The hole concentrations of $Cu_{2-x}S$ can vary in at least two orders of magnitude on tailoring the contents of Cu vacancies[19,29]. By contrast, foreign atoms are hard to enter into the lattice of superionic conductor materials, thus the effect of extrinsic doping on carrier concentration adjustment is not obvious[30]. In addition, compositing with second phase benefits to further enhance the phonon scattering for reducing thermal conductivity, extra particles are also capable of blocking long-range migration of Cu ions for improving stability of copper sulfides[31]. It has been reported that both Sn doping and Se alloying could improve the thermoelectric performance of copper sulfides owing to the porous microstructure and tuned bonding energy[32–35]. Previous works have also investigated that compositing with multi-walled carbon nanotube[28] or grapheme[26] are effective in improving thermoelectric performance of copper sulfides by decreasing lattice thermal conductivity. Additionally, $Cu_{2-x}S$ phase-junction nanocomposites with superior thermoelectric performance can be synthesized by surface-ligand tuning[36], indicating that carefully adjusting Cu vacancies benefits to optimize the thermoelectric properties. Nevertheless, the electrical stability of these materials has not been studied in detailed, and the method of spontaneously introducing Cu vacancies and in-situ generated precipitates according to the designed composition by one-pot approach have not reported yet.

Herein, a one-pot modulation strategy for simultaneously adjusting carrier and phonon transport in copper sulfides is proposed as shown in Fig. 1. The first step aims at in-situ generating Cu_2SnSe_4 precipitates and various lattice defects by adding a suitable content of Sn and Se in Cu_2S, benefiting for strengthening the phonon scattering. The lattice thermal (κ_l) conductivity at 873 K is therefore significantly lowered (Fig. 1b). Second, additional Se is added to further introduce the Cu vacancies and reduce the bond energy in the material. Tuning the Cu content can regulate the hole concentration and the temperature of the phase transition, then the highly enhanced average power factor ($PF_{ave.}$) is therefore realized (Fig. 1c). Cu vacancies are the key factors of optimizing the electrical conductivity and stability of copper sulfides, whereas the multiscale lattice defects act as the key roles in overall reducing lattice thermal conductivity of the materials. Compositional regulation and structural evolution are simultaneously realized by the two-step optimization, benefiting for synergistically improving thermoelectric performance. As a result, the ZT of the $Cu_{1.992}SSe_{0.016}(Cu_2SnSe_4)_{0.004}$ specimen reaches approximately 1.6 at 873 K, which is comparable to that of other Cu-based thermoelectric materials (Cu_2Se, Cu_2Te) at the same temperature (Fig. 1d)[19,24,37–40]. Furthermore, the electrical stability and mechanical performance of this sample are significantly enhanced. This strategy may also work for enhancing thermoelectric performance in other superionic conductors.

Results and discussion

The phase structures of the Cu_2S, $Cu_{1.992}S(Cu_2SnSe_4)_{0.004}$ and $Cu_{1.992}SSe_{0.016}(Cu_2SnSe_4)_{0.004}$ bulk specimens were characterized by X-ray diffraction (XRD), as shown in Fig. 2. The diffraction peaks of the pristine sample can be indexed to the monoclinic Cu_2S phase (PDF#83-1462). Furthermore, the main phase changes to tetragonal $Cu_{1.96}S$ (PDF#29-0578) after introducing a suitable content of Sn and Se by one-pot modulation, indicating the generation of Cu vacancies in the matrix. The added Sn and Se prefer to consume Cu to form the Cu_2SnSe_4 second phase and generate a tiny content of Cu vacancies. There are diffraction peaks of Cu_2SnSe_4, verifying that the reaction occurred during the synthesis process. Notably, the characteristic peaks of the $Cu_{1.992}SSe_{0.016}(Cu_2SnSe_4)_{0.004}$ specimen shift toward a higher 2θ than those of the $Cu_{1.992}S(Cu_2SnSe_4)_{0.004}$ sample. The lattice shrinkage implies that more Cu vacancies are produced after adding additional Se. Excess Se can easily enter into the lattice of copper sulfides matrix, which have been proved in the previous studies[32,39]. The relative density of the bulk materials synthesized by one-pot modulation first decreases and then gradually increases with additive content, indicating the generation of a tiny content of pores, which might then be filled in by precipitates. The density of the bulk materials remains at a high level (Supplementary Fig. 1 and Supplementary Table 1).

The fracture morphology of all samples is exhibited in Supplementary Fig. 2. The transgranular fracture of the pure sample gradually shifts to intergranular fracture with increasing addition content, corresponding to the stratiform fractured surface changing to particle-like grains. Additionally, pores are generated along the grain boundaries and within the grains for the samples fabricated by one-pot modulation, which is mainly ascribed to the partial sulfur volatilization in the Cu-deficient copper sulfides. The content of pores in the materials is in good agreement with the change in density. Subsequently, microscale precipitates can be visualized in the material, which mainly exist along the grain boundaries. An electron probe microanalyzer

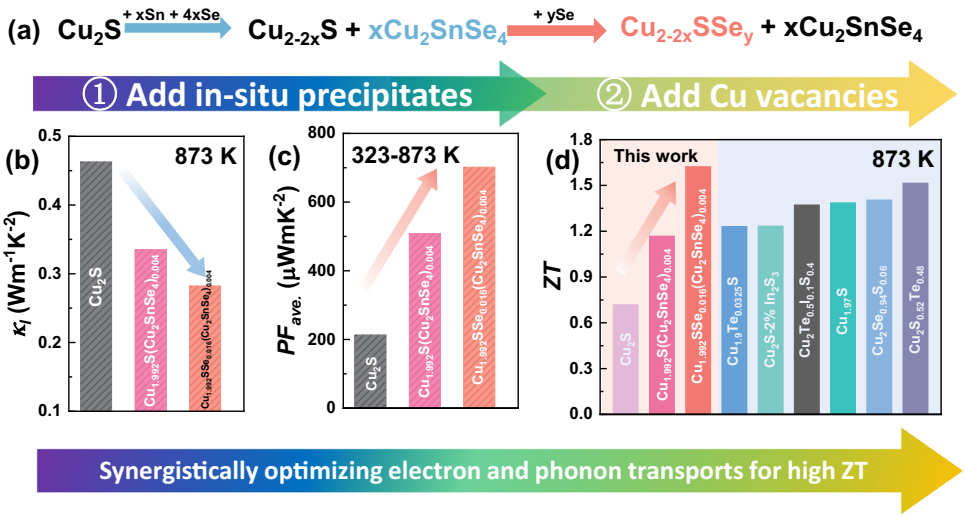

Fig. 1 | The designed one-pot strategy of utilizing second phase and Cu vacancies modulation to optimize thermoelectric properties of copper sulfides. a The process of a one-pot modulation strategy in adjusting electrical and thermal transport properties. **b** Lattice thermal, (**c**) average power factor and (**d**) ZT of Cu_2S, $Cu_{1.992}S(Cu_2SnSe_4)_{0.004}$ and $Cu_{1.992}SSe_{0.016}(Cu_2SnSe_4)_{0.004}$ bulk samples. Peak ZT values at 873 K for other copper-based thermoelectric materials are added for comparison, and the data were taken from refs. 19,24,37–40.

https://doi.org/10.1038/s41467-024-47148-0

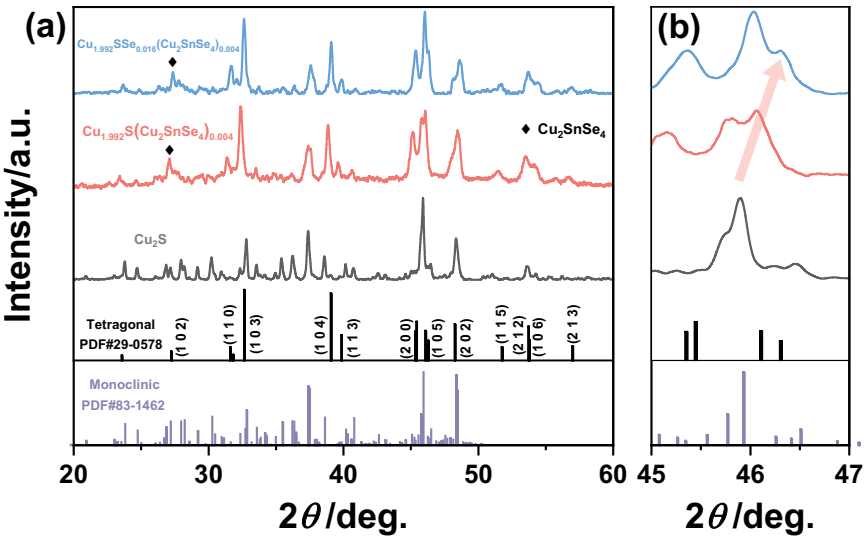

Fig. 2 | Phase structure characterization of copper sulfide-based materials. a XRD patterns of the Cu_2S, $Cu_{1.992}S(Cu_2SnSe_4)_{0.004}$ and $Cu_{1.992}SSe_{0.016}(Cu_2SnSe_4)_{0.004}$ bulk samples. **b** Enlarged XRD patterns of the Cu_2S, $Cu_{1.992}S(Cu_2SnSe_4)_{0.004}$ and $Cu_{1.992}SSe_{0.016}(Cu_2SnSe_4)_{0.004}$ bulk samples at 45°–47°.

(EPMA) was utilized to observe the distribution of pores and precipitates among the $Cu_{1.992}SSe_{0.016}(Cu_2SnSe_4)_{0.004}$ sample, as shown in Supplementary Fig. 3. Energy-dispersive spectroscopy (EDS) spot scanning was performed for the visualized second phase particles with different grain sizes, suggesting that the multiscale precipitates would be Cu_2SnSe_4. Partial large-scale precipitates are distributed along the grain boundaries, while the nanoprecipitates fill in the nanopores. The special nanostructures of nanoprecipitates embedded in nanopores can usually observed in copper chalcogenides owing to the element emission and the existence of a suitable substrate for crystal growth[41,42]. In addition, the decreased Cu content of the matrix after adding extra Se can be confirmed by the EPMA as well (Supplementary Fig. 4). The existence of these lattice defects is the main reason for the grain refinement in this study, the pores and inclusions can inhibit the migration of grain boundaries.

To further observe the nanoscale lattice defects, TEM was performed for the $Cu_{1.992}SSe_{0.016}(Cu_2SnSe_4)_{0.004}$ bulk sample. A high-angle annular dark field (HAADF) image is shown in Fig. 3a, nanopores and nanoprecipitates are easily distinguished. Nanoprecipitates were observed in the TEM image, which consist of Cu, Sn and Se by EDS mapping (Supplementary Fig. 5). Therefore, the introduction of the suitable content of Sn and Se in copper sulfide can produce the Cu_2SnSe_4 nanoprecipitates. But the precipitates are highly possibly just covered by the matrix without really exposed, and it is too thin comparing with the matrix in the characterization region. It is therefore hard to clearly show the lattice of the Cu_2SnSe_4 from FFT pattern and/or HRTEM fringe due to the strong effects of the matrix lattices. It can be reasonable proposed that the interfaces between Cu_2S and Cu_2SnSe_4 are incoherent due to their different crystal structures. According to the enlarged TEM image shown in Fig. 3c, there is the region of high-density dislocations, which can be observed through the inverse fast Fourier transform (Fig. 3e). The distribution of a mass of dislocations is consistent with the local concentrated stress by geometric phase analysis (Fig. 3f). The bright parts imply that local concentrated stress exists around the dislocations, which is effective in scattering mid-frequency phonons and restrains the lattice thermal conductivity in the medium temperature range[43,44]. In addition to the noticeable high-density dislocation area, concentrated stress is different from the pristine Cu_2S (Supplementary Fig. 6). The lattice stress originates from the structural evolution induced by compositional regulation. First, Cu vacancies are produced in the copper sulfide after introducing a refined ratio of additives, resulting in the formation of edge dislocations in the matrix and significant lattice distortion[45]. In addition, a mass of interfaces are introduced in the material owing to the grain refinement and the additional nanoprecipitates and nanopores, the lattice stress is also triggered by the dislocations distributed around the interfaces[46]. As shown in Fig. 3g, Cu vacancies in copper sulfide can diffuse and form vacancy clusters during annealing. There are closed rings of edge dislocations when these vacancy clusters further collapse. Higher vacancy concentration would promote the dislocation climbing, resulting in a higher dislocation density. Furthermore, tetragonal and monoclinic phases coexist in the materials near room temperature, which gradually change to hexagonal and then cubic phases with temperature. Obvious atomic mismatch caused by multiphase coexistence leads the strain of compression and extension, and a similar phenomenon is ubiquitous in our samples. In summary, multiscale second phase, refined grains, nanopores and dislocations are introduced in the one-pot modulated copper sulfide-based material, which contribute to scatter heat carriers.

The temperature dependence of the electrical transport properties of the Cu_2S, $Cu_{1.992}S(Cu_2SnSe_4)_{0.004}$ and $Cu_{1.992}SSe_{0.016}(Cu_2SnSe_4)_{0.004}$ bulk specimens is exhibited in Fig. 4. The electrical conductivity (σ) gradually increases with temperature and then decreases after undergoing the phase transition temperature (Fig. 4a), indicating that the semiconductor behavior changes to metallic-like behavior. The two turning points of σ gradually shift to lower temperatures after introducing refined Sn and Se. Monoclinic Cu_2S and tetragonal $Cu_{1.96}S$ coexist in the $Cu_{1.992}S(Cu_2SnSe_4)_{0.004}$ and $Cu_{1.992}SSe_{0.016}(Cu_2SnSe_4)_{0.004}$ samples, different phase structures affect the turning points of the electrical and thermal transport properties. The increased content of tetragonal $Cu_{1.96}S$ results in the enlarged temperature window for achieving high power factor, benefiting for improving average thermoelectric performance. Differential Scanning Calorimetry (DSC) curves of the pristine Cu_2S and $Cu_{1.992}SSe_{0.016}(Cu_2SnSe_4)_{0.004}$ samples indicate that the introduction of Cu vacancies can decrease the temperature of phase transition for copper sulfides (Supplementary Fig. 7). It is worth noting that the σ of $Cu_{1.992}SSe_{0.016}(Cu_2SnSe_4)_{0.004}$ is further improved compared to that of the $Cu_{1.992}S(Cu_2SnSe_4)_{0.004}$ sample, which is due to the progressive enhancement in hole concentration by introducing more Cu vacancies. Additionally, the Seebeck coefficient (S) of $Cu_{1.992}S(Cu_2SnSe_4)_{0.004}$ sample obviously drops by comparison of that of the pure Cu_2S specimen because of the variation in carrier concentration (Fig. 4b). Additionally, S further reduces after introducing

https://doi.org/10.1038/s41467-024-47148-0

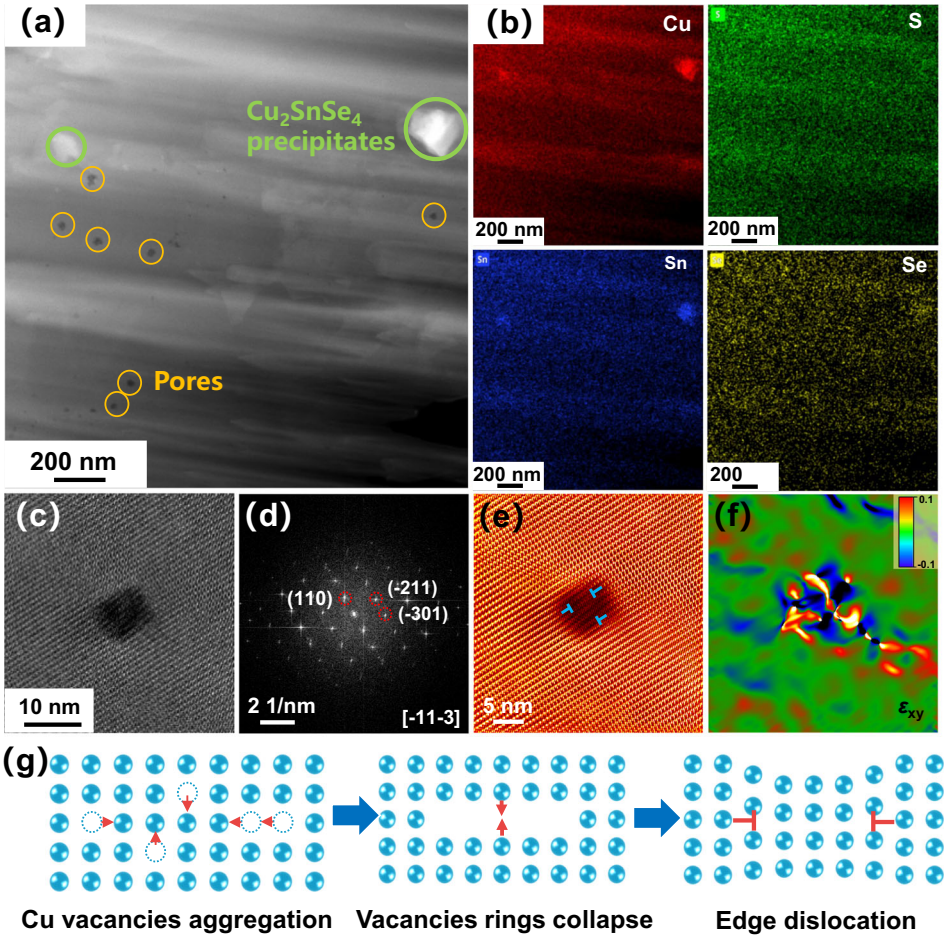

Fig. 3 | STEM characterization of the $Cu_{1.992}SSe_{0.016}(Cu_2SnSe_4)_{0.004}$ bulk specimen. a HAADF image exhibits the existence of precipitates and nanopores in the material. **b** EDS element mapping of the area in (**a**), indicating that precipitates in the bulk composite are Cu_2SnSe_4. **c** High-resolution TEM (HRTEM) image of the $Cu_{1.992}SSe_{0.016}(Cu_2SnSe_4)_{0.004}$ bulk specimen, expressing the existence of a high-density dislocation area. **d** Corresponding fast Fourier transform (FFT) image of the area, (**e**) the inverse fast Fourier transform (IFFT) image at the selected area. **f** The stress distribution of the whole region in (**c**) by geometric phase analysis (GPA), and the color bar represents −10% to 10% strain. **g** Schematic diagram of the formation of edge dislocation by Cu vacancy.

extra Se, which still remains at a high-level owing to the enhanced carrier effective mass after alloying with Se (Fig. 4e). For the $Cu_{1.992}SSe_{0.016}(Cu_2SnSe_4)_{0.004}$ specimen, an S of 196 μVK^{-1} and a σ of 377 S cm^{-1} are obtained at 873 K. The electrical transport properties for other $Cu_{2-2x}SSe_{4x}(Cu_2SnSe_4)_x$ samples are exhibited in Supplementary Fig. 8. To further investigate the effects of the second phase and Cu vacancies on the charge transport of copper sulfides, Hall measurements and optical band gaps were performed. Figure 4c expresses the carrier concentration (n_H) and mobility (μ_H) of the Cu_2S, $Cu_{1.992}S(Cu_2SnSe_4)_{0.004}$ and $Cu_{1.992}SSe_{0.016}(Cu_2SnSe_4)_{0.004}$ samples at room temperature. As predicted, the n_H reaches 11.09×10^{20} cm^{-3} for the $Cu_{1.992}SSe_{0.016}(Cu_2SnSe_4)_{0.004}$ sample, which is dramatically higher than that of both pristine Cu_2S sample (0.08×10^{20} cm^{-3}) and $Cu_{1.992}S(Cu_2SnSe_4)_{0.004}$ sample (2.57×10^{20} cm^{-3}). Herein, introduced Cu vacancies are the main reason for the increase in hole concentration. μ_H gradually drops from 21.46 $cm^2V^{-1}s^{-1}$ for Cu_2S to 2.03 $cm^2V^{-1}s^{-1}$ for the $Cu_{1.992}SSe_{0.016}(Cu_2SnSe_4)_{0.004}$ specimen. Extra interfaces introduced by grain refinement and pores can deteriorate the carrier transport. The n_H and μ_H for the $Cu_{1.992}SSe_{0.016}(Cu_2SnSe_4)_{0.004}$ sample within a temperature range of 323–873 K were also characterized (Supplementary Fig. 9). Copper sulfides are degenerate semiconductors, thus, there is only a slight variation in carrier concentration for $Cu_{1.992}SSe_{0.016}(Cu_2SnSe_4)_{0.004}$ with temperature. Carrier mobility gradually drops with temperature due to the scattering effects of lattice vibration and Cu ion migration. The electronic structures, total density of states and partial density of states for Cu_2S and $Cu_{1.96}S$ were calculated based on the optimized crystal structure (Supplementary Fig. 10), implying a typical Dirac cone structure that is in agreement with the previously calculated results[47]. For $Cu_{1.96}S$, Cu vacancies shift the valence band maximum (VBM) upward the conduction band minimum and hence lead to an increased hole concentration. The band shape is almost maintained after introducing Cu vacancies, which is mainly determined by the S sublattice[48]. Furthermore, the optical band gap (E_g) for the samples is shown in Fig. 4d, and E_g widens with addition content. Cu vacancies in the copper sulfides can reduce the antibonding character and thus lower the energy position of the VBM[47]. The relationships between the Seebeck coefficient and carrier concentration are fitted by a single parabolic band (SPB) model and depicted in Fig. 4e. The density of states (DOS) effective mass (m^*) of the $Cu_{1.992}SSe_{0.016}(Cu_2SnSe_4)_{0.004}$ samples is obviously larger than that of pure Cu_2S at room temperature, and the m^* of the $Cu_{1.992}SSe_{0.016}(Cu_2SnSe_4)_{0.004}$ sample reaches 2.41 m_O at 873 K, which favors maintaining the Seebeck coefficient due to the enhanced DOS near the Fermi level. Owing to the sharp increase in electrical conductivity by inducing Cu vacancies in the material, the power factor (PF) for all $Cu_{1.992}SSe_{0.016}(Cu_2SnSe_4)_{0.004}$ samples is improved, as shown in Fig. 4f. A peak PF of 1450 $\mu Wm^{-1}K^{-2}$ is attained at 873 K for the $Cu_{1.992}SSe_{0.016}(Cu_2SnSe_4)_{0.004}$ specimen. More importantly, a higher power factor is realized at a lower temperature for our bulk specimens. Cu vacancies and precipitates induced by one-pot

https://doi.org/10.1038/s41467-024-47148-0

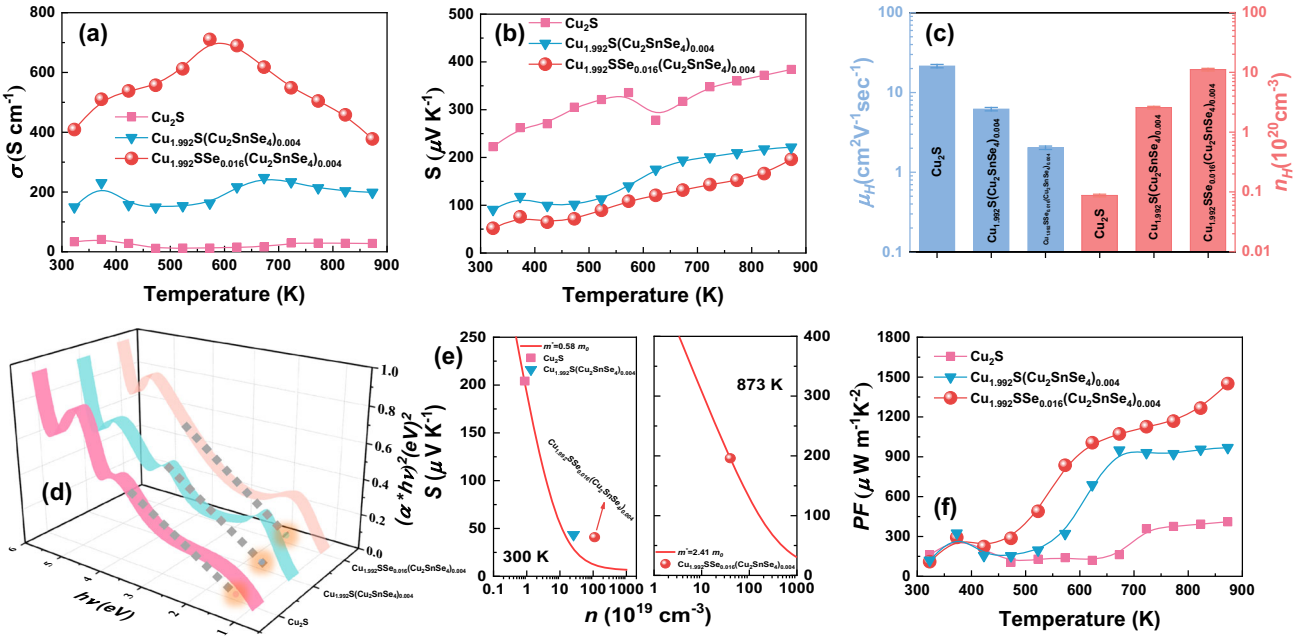

Fig. 4 | Electrical transport properties of Cu_2S, $Cu_{1.992}S(Cu_2SnSe_4)_{0.004}$ and $Cu_{1.992}SSe_{0.016}(Cu_2SnSe_4)_{0.004}$ bulk samples. Temperature dependence of (**a**) electrical conductivity, (**b**) Seebeck coefficient and (**f**) power factor of Cu_2S, $Cu_{1.992}S(Cu_2SnSe_4)_{0.004}$ and $Cu_{1.992}SSe_{0.016}(Cu_2SnSe_4)_{0.004}$ bulk samples. **c** Composition-dependent hall carrier concentration and mobility at 300 K for all bulk samples. **d** $(\alpha h\upsilon)^2$ vs. $h\upsilon$ of all specimens, the optical band gap (E_g) can be estimated by extrapolating the straight line to $(\alpha h\upsilon)^2 = 0$. **e** Seebeck coefficient as a function of carrier concentration at 300 K and 873 K. Red lines are obtained by the SPB model and estimating the carrier effective mass, and dots are obtained by experimental data.

modulation facilitate medium-temperature thermoelectric materials to possess larger output power in a wider temperature range.

Figure 5 presents the temperature dependence of the thermal transport properties for Cu_2S, $Cu_{1.992}S(Cu_2SnSe_4)_{0.004}$ and $Cu_{1.992}SSe_{0.016}(Cu_2SnSe_4)_{0.004}$ bulk specimens. The total thermal conductivity (κ) of the $Cu_{1.992}SSe_{0.016}(Cu_2SnSe_4)_{0.004}$ sample is larger than that of the pristine Cu_2S material over the whole temperature range, as shown in Fig. 5a. κ is 0.85 $Wm^{-1}K^{-1}$ (323 K) and 0.78 $Wm^{-1}K^{-1}$ (873 K) for $Cu_{1.992}SSe_{0.016}(Cu_2SnSe_4)_{0.004}$, respectively. To determine the reason for the variation in thermal conductivity, the electronic thermal conductivity (κ_e) of all specimens is calculated by the Wiedeman-Franz law (Supplementary Fig. 11), and the lattice thermal conductivity is evaluated by subtracting κ_e from κ. The tendency of κ_e in the specimens is similar to that of the electrical conductivity, and there is an order of magnitude difference in κ_e between the Cu_2S and $Cu_{1.992}SSe_{0.016}(Cu_2SnSe_4)_{0.004}$ specimens. Therefore, obviously increased carrier concentration and enhanced electrical conductivity are the main reasons for the total thermal conductivity enhancement. Nevertheless, the κ_l of $Cu_{1.992}SSe_{0.016}(Cu_2SnSe_4)_{0.004}$ samples is lower than that of the pristine Cu_2S material, which stems from the existence of various lattice defects in the bulk specimen, contributing to significantly scattering the mid-to-short frequency phonon. As shown in Fig. 5c, the κ_l curves for the specimens under different states were modeled to evaluate the effects of multiscale lattice defects on decreasing lattice thermal conductivity by the Debye-Callaway model. Umklapp (U), interface (I), precipitates (P), nanoprecipitates (NP) and dislocation (D) scattering are considered[49,50]. The calculation details, including equations, modulus, grain size, and density of dislocations and precipitates observed by TEM, can be seen in Supplementary Table 2. However, after considering the Umklapp process, various interfaces, multiscale precipitates and dislocation cores and strain, the predicted curve only approximately matches the experimental lattice thermal conductivity of the $Cu_{1.992}SSe_{0.016}(Cu_2SnSe_4)_{0.004}$ sample at high temperature. The obvious deviation at low temperature might be related to the different crystal structures of copper sulfide-based materials, which would affect the phonon transport, in particular, the Cu vacancies and the different positions of Cu^+ ions. This simulation is close to the lattice thermal conductivity calculated by Cahill's theory[51], indicating the great contribution of multiple structural defects to phonon scattering. Because of the strong phonon scattering effect and low-frequency localized vibrations caused by disordered Cu^+ ion migration and Cu vacancies, the lattice thermal conductivity of copper sulfides is intrinsically low, and the contributions of multiscale lattice defects to lattice thermal conductivity reduction are not as obvious as those in other materials. The frequency dependence of the lattice thermal conductivity of the $Cu_{1.992}SSe_{0.016}(Cu_2SnSe_4)_{0.004}$ sample is plotted in Supplementary Fig. 12 to better understand the influence of different mechanisms. The Umklapp process, extra grain boundaries and pore interfaces are responsible for scattering low- to medium-frequency phonons for lowering the lattice thermal conductivity at low temperature. The dislocation cores and strain can strongly scatter phonon with mid frequencies to reduce the lattice thermal conductivity at medium temperature, endowing copper sulfides higher thermoelectric performance. In addition, the sound velocities of all specimens were characterized and are exhibited in Fig. 5d. The longitudinal sound speed (υ_l) gradually increases after adding Sn and Se by one-pot modulation owing to the enhanced bulk density of specimens, but the transverse sound velocity (υ_t) decreases. Se-alloying has been proved to be effective in reducing bonding energy of the Cu_2S materials, resulting in the decreased speed of sound and therefore the lower lattice thermal conductivity[37]. Ultimately, although the increased hole concentration and electrical conductivity lead to enhanced carrier thermal conductivity, highly strengthened phonon scattering by various mechanisms assists the ultralow lattice thermal conductivity and the maintained total thermal conductivity.

Benefiting from the significantly enhanced electrical transport properties and the maintained thermal conductivity, an overall improved thermoelectric figure of merit (ZT) is realized for the one-pot modulated samples (Supplementary Fig. 13). A peak ZT beyond 1.6 is achieved for the $Cu_{1.992}SSe_{0.016}(Cu_2SnSe_4)_{0.004}$ sample at 873 K (Fig. 6a). According to the experimental carrier concentration and mobility and lattice thermal conductivity at different temperatures,

https://doi.org/10.1038/s41467-024-47148-0

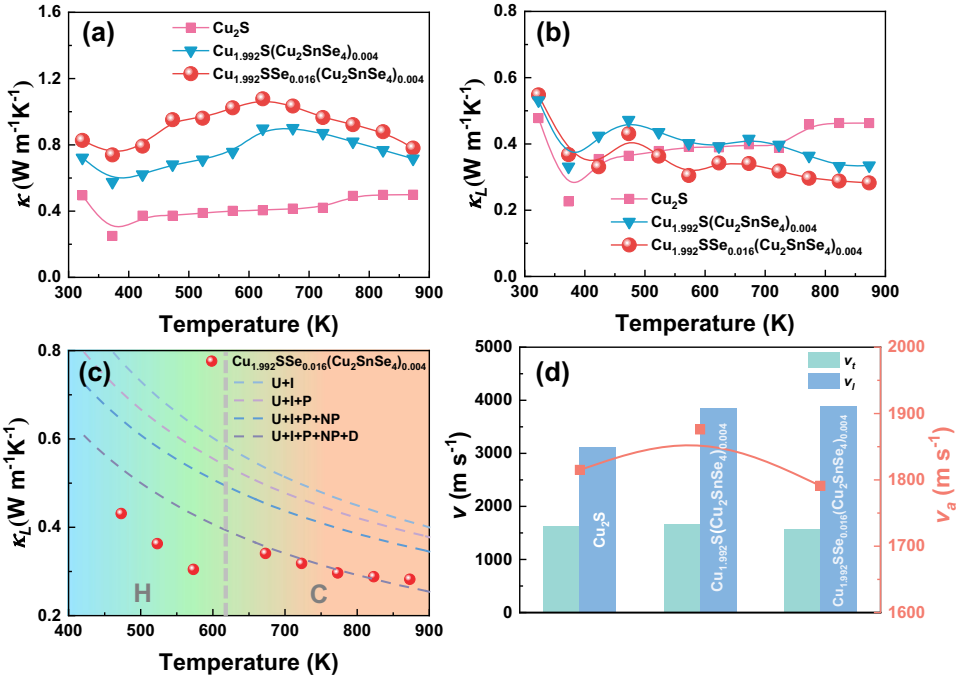

Fig. 5 | Thermal transport properties of copper sulfide-based bulk composites. Temperature dependence of (**a**) thermal conductivity and (**b**) lattice thermal conductivity for Cu_2S, $Cu_{1.992}S(Cu_2SnSe_4)_{0.004}$ and $Cu_{1.992}SSe_{0.016}(Cu_2SnSe_4)_{0.004}$ bulk samples. **c** Fitting lattice thermal conductivity by the Callaway thermal conductivity model. **d** Sound velocity of Cu_2S, $Cu_{1.992}S(Cu_2SnSe_4)_{0.004}$ and $Cu_{1.992}SSe_{0.016}(Cu_2SnSe_4)_{0.004}$ bulk samples.

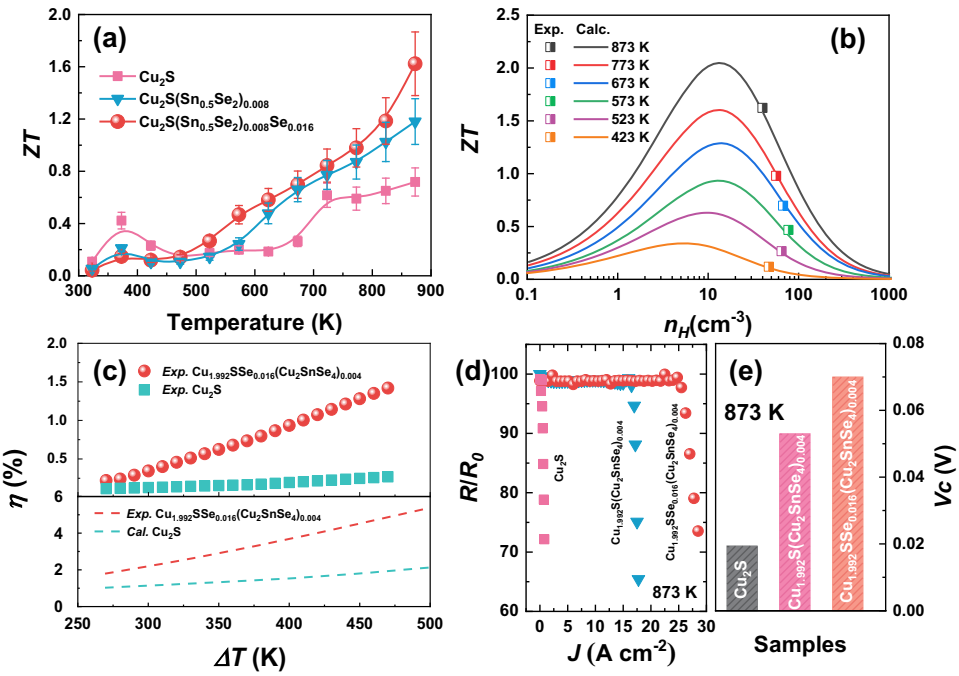

Fig. 6 | Thermoelectric performance of copper sulfide-based bulk composites. Temperature dependence of (**a**) dimensionless figure of merit *ZT* of Cu_2S, $Cu_{1.992}S(Cu_2SnSe_4)_{0.004}$ and $Cu_{1.992}SSe_{0.016}(Cu_2SnSe_4)_{0.004}$ bulk samples. **b** Carrier concentration dependence of the *ZT* value at different temperatures by using the SPB model. **c** Experimental and estimated conversion efficiency as a function of temperature gradient for the $Cu_{1.992}SSe_{0.016}(Cu_2SnSe_4)_{0.004}$ sample. **d** Related electrical resistivity (R/R_0) of the $Cu_{1.992}SSe_{0.016}(Cu_2SnSe_4)_{0.004}$, $Cu_{1.96}S$ and Cu_2S samples with increased current density at 873 K. **e** The critical voltage (V_c) of the pristine Cu_2S and that with Sn and Se addition at 873 K.

the *ZT* values of the $Cu_{1.992}SSe_{0.016}(Cu_2SnSe_4)_{0.004}$ sample are expressed as a function of carrier concentration in Fig. 6b, which are located at the theoretical lines simulated by the SPB model. Nevertheless, the excessive carrier concentration caused by the induced Cu vacancies results in the actual *ZT* being lower than the theoretical value. Therefore, the $Cu_{1.992}SSe_{0.016}(Cu_2SnSe_4)_{0.004}$ material still has great potential to achieve higher *ZT* by further introducing n-type dopants or decreasing the bonding energy. The temperature gradient (ΔT) dependence of the conversion efficiency of the $Cu_{1.992}SSe_{0.016}(Cu_2SnSe_4)_{0.004}$ sample is calculated (η_{cal}) after

https://doi.org/10.1038/s41467-024-47148-0

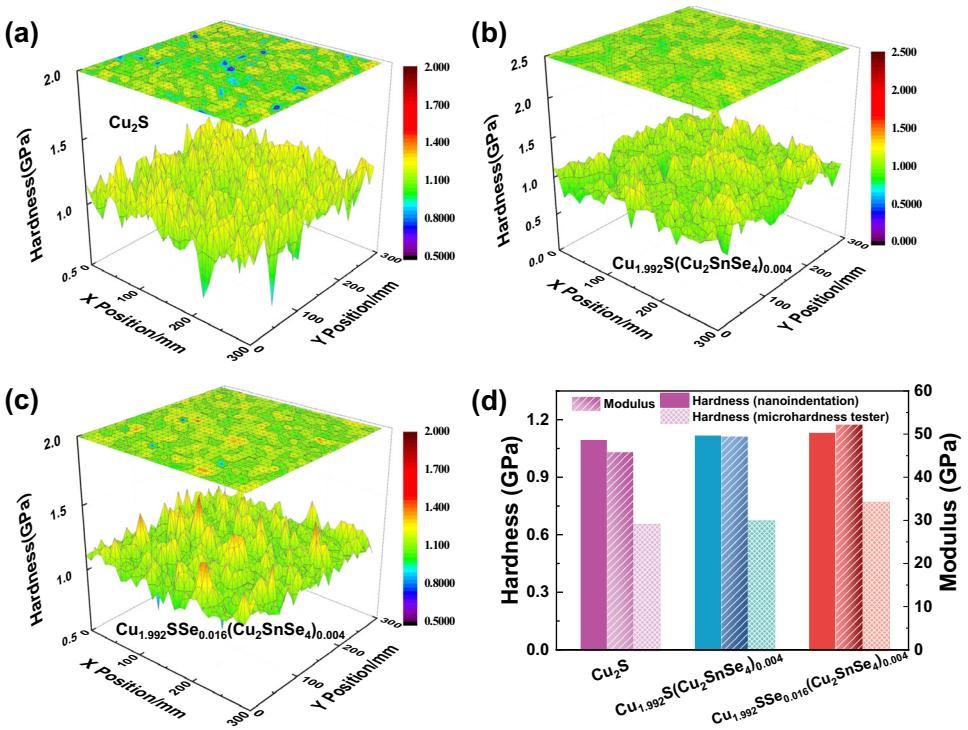

Fig. 7 | Mechanical performance of copper sulfide-based bulk samples. 3D cloud diagram of hardness for (**a**) pure Cu_2S, (**b**) $Cu_{1.992}S(Cu_2SnSe_4)_{0.004}$ and (**c**) $Cu_{1.992}SSe_{0.016}(Cu_2SnSe_4)_{0.004}$ bulk samples. **d** Average modulus and average hardness of Cu_2S, $Cu_{1.992}S(Cu_2SnSe_4)_{0.004}$ and $Cu_{1.992}SSe_{0.016}(Cu_2SnSe_4)_{0.004}$ samples measured by using a nanoindentation instrument and microhardness tester, respectively.

considering the Thomson heat, as shown in Fig. 6c[52]. With a cold-side temperature of 300 K, the $Cu_{1.992}SSe_{0.016}(Cu_2SnSe_4)_{0.004}$ sample yields an η_{cal} greater than 5% when ΔT reaches 470 K, which is approximately three times higher than that of the pristine Cu_2S sample. The power generation efficiency (η_{exp}) of the fabricated single-leg thermoelectric modules by $Cu_{1.992}SSe_{0.016}(Cu_2SnSe_4)_{0.004}$ material is measured by mini-PEM, as shown in Fig. 6c. The current-dependent voltage (V), output power (P), heat flux (Q) and conversion efficiency at different hot-side temperatures for the single-leg TE module are shown in Supplementary Fig. 14. Because of the contact resistance between the electrode and TE module, the measured efficiency is overall lower than the evaluated efficiency. A η_{exp} of 1.5% is obtained at a temperature difference of 470 K, which is still higher than that of the module consisting of pure Cu_2S because of the enhanced average ZT.

Electrical stability is also important in practical device applications and can be evaluated by the relative resistance (R/R_O) of the $Cu_{1.992}SSe_{0.016}(Cu_2SnSe_4)_{0.004}$ and $Cu_{1.992}S(Cu_2SnSe_4)_{0.004}$ samples under increased current density at 873 K by comparison of the pure Cu_2S material. The R/R_O for the pristine Cu_2S material dramatically decreases after starting subjecting a small current density, indicating poor electrical stability and material failure under an electrical field (Fig. 6d). The critical current density (J_c) indicates the strength of the external field that enables the concentration of Cu^+ ions in the Cu-based superionic conductors to meet the chemical potential for metallic Cu deposition. A higher J_c is obtained for the $Cu_{1.992}S(Cu_2SnSe_4)_{0.004}$ material compared with the Cu_2S sample under the same conditions owing to the inhabitation of long-range migration of Cu ion by the precipitates. Additionally, R/R_O for the $Cu_{1.992}SSe_{0.016}(Cu_2SnSe_4)_{0.004}$ sample drops until the current density reaches approximately 25 A cm^{-2}, suggesting that the introduced Cu vacancies by adding extra Se in the copper sulfides are beneficial for decreasing the concentration of Cu ions and optimizing the stability of copper sulfides. Furthermore, in order to more reasonably evaluate the electrical stability of the superionic conductors, the critical voltage (V_c) of the $Cu_{1.992}SSe_{0.016}(Cu_2SnSe_4)_{0.004}$ and $Cu_{1.992}S(Cu_2SnSe_4)_{0.004}$ samples at 873 K are shown in Fig. 6e, the calculated details can be seen in the reported works[53]. V_c of the pristine Cu_2S is slightly lower than the reported result due to the higher measurement temperature. Besides, higher V_c of $Cu_{1.992}SSe_{0.016}(Cu_2SnSe_4)_{0.004}$ indicates that the spontaneously generated Cu vacancies and multiscale precipitates contribute to improve the electrical stability of copper sulfides. Owing to the introduction of Cu vacancies and precipitates in the copper sulfides, the thermoelectric performance of the Sn and Se-added samples is maintained in the cycling test (Supplementary Fig. 15).

The mechanical performance of all bulk specimens was characterized by nanoindentation with the Nano-Blitz 3D method (Supplementary Fig. 16). 3D diagrams of hardness (H) (Fig. 7a–c) suggest that H for the $Cu_{1.992}SSe_{0.016}(Cu_2SnSe_4)_{0.004}$ sample is obviously higher than that of both the Cu_2S and $Cu_{1.992}S(Cu_2SnSe_4)_{0.004}$ bulk samples. The average hardness and modulus of the bulk composites are plotted in Fig. 7d. Gradually enhanced mechanical properties are ascribed to grain refinement and dispersion strengthening. A large number of grain boundaries and second phase interfaces are introduced by one-pot modulation, which are capable of blocking the dislocation motion and enhancing the hardness of composites. The Vickers hardness of the composites is also characterized by a microhardness tester (Fig. 7d). The similar tendency of microhardness but lower values compared with H measured by nanoindentation (Fig. 7d and Supplementary Fig. 17) reflect those widespread pores in the $Cu_{1.992}SSe_{0.016}(Cu_2SnSe_4)_{0.004}$ samples weaken the overall hardness of the materials. The enhanced mechanical performance of composites by structural and compositional evolution would promote copper sulfides further engaging as p-type legs in thermoelectric device assembly.

In summary, XRD, FESEM, EMPA, EDS and TEM results demonstrate that employing one-pot modulation to fabricate copper sulfide-based materials can introduce an in-situ generated precipitates while effectively tuning the Cu content for synergistically improving thermal

and electrical properties. Multiscale precipitates, nanopores and dislocations are produced in the specimens, an ultralow lattice thermal conductivity is obtained through strengthening the phonon scattering effect by various mechanisms. Meanwhile, the introduced Cu vacancies have significant potential for improving electrical conductivity while reducing the phase transition temperature, and an overall and obviously improved power factor is realized. Ultimately, a peak ZT of 1.6 is obtained for the $Cu_{1.992}SSe_{0.016}(Cu_2SnSe_4)_{0.004}$ bulk sample at 873 K. The introduced precipitates and Cu vacancies can also suppress Cu ion migration and improve the electrical stability of Cu-based superionic conductors. Therefore, this one-pot modulation promotes copper sulfide-based composites as potential candidates for thermoelectric applications, which is worth facilitating in other material systems.

Methods

Synthesis

Cu_2S, $Cu_{1.992}S(Cu_2SnSe_4)_{0.004}$ and $Cu_{2-2x}SSe_{4x}(Cu_2SnSe_4)_x$ ($x = 0$, 0.003, 0.0035, 0.004, 0.005 and 0.006) materials were fabricated by high-temperature melting, long-time annealing, high-energy ball milling and spark plasma sintering. High-purity raw elements, Cu (pellet bulk, 99.999%), S (pellet, 99.999%), Sn (pellet, 99.999%) and Se (pellet, 99.999%), were weighed out according to the stoichiometric proportions, placed in a quartz tube, and then the tube was evacuated at 10^{-4} Pa and sealed. The samples were heated to 1373 K in 18 h, keeping at 1373 K for 12 h, and then cooled to 1073 K within 24 h. The annealing process is holding at 1073 K for 7 days and then cooling to 300 K by shutting down the furnace power. The obtained ingots were grinded into fine powders under a protective atmosphere condition (95 vol% Ar) by ball-milling (Retsch Emax, German) for 30 min with a speed of 800 rpm. The prepared powders were put into a graphite mold with the size of φ20 mm, which was sintered at 773 K under 50 MPa pressure in 5 min by using the spark plasma sintering system (Sumitomo SPS1050, Japan). The bulk samples were subsequently cut and polished.

Characterization

X-ray diffraction (XRD MiniFlex600 Rigaku, Japan) was utilized to detect the phase structure of the prepared bulk samples from diffraction angles from 20° to 60° at a speed of 5°/min by using Cu Kα radiation ($\lambda = 1.54$ Å). The morphologies of the fractured bulk samples were inspected using electron probe microanalysis (EPMA, JEOL, JXA-8230, Japan) and field emission scanning electron microscopy (FESEM, ZEISS, Sigma 300, Germany) equipped with energy dispersive spectroscopy (EDS, JED-2300T). Scanning transmission electron microscopy (STEM, FEI Titan) was utilized to investigate the microstructures and nanoprecipitates in the bulk samples. The electrical conductivity (σ) and the Seebeck coefficient (S) were simultaneously measured by a resistivity and Seebeck coefficient measurement system (ZEM-3, Advance Riko, Japan) in a low-pressure helium gas environment. Additionally, the thermal conductivity (κ) of the bulk composites was calculated by $\kappa = D \times C_p \times \rho$, where the thermal diffusivity D was measured using an LFA457 (Netzsch, Germany) laser flash apparatus, the specific heat (C_p) was calculated using $C_p = 3Nk_B$, and the mass density ρ was measured by the Archimedes method. The DSC curves of the samples in the temperature range of 310–773 K are obtained by the Netzsch STA 449 F3 (Germany) instrument under flowing Ar gas, and the heating speed is 10 K min^{-1}. The Hall carrier concentration (n_H) and mobility (μ_H) of the thin samples were tested by using a Hall effect measurement system (Ecopia, HMS-7000, Korea). The microhardness (H) and Young's modulus (E) of all bulk samples were measured by utilizing a nanoindenter, 900 points were presses on the polished surface of samples, and a target load of 20 mN and a feature height of 2000 nm were set (iMicro KLA., USA). The relative resistivity of the $Cu_{1.992}SSe_{0.016}(Cu_2SnSe_4)_{0.004}$ bulk sample was measured by a homemade instrument including a vacuum furnace and an electrochemical station. The absolute error of all experimental data can be assumed to be 3%–4%, so the error bar of ZT would be 15%–20%.

Data availability

The data that support the findings of this study are available from the corresponding author on request.

References

1. Xiao, Y. & Zhao, L.-D. Seeking new, highly effective thermoelectrics. *Science* **367**, 1196–1197 (2020).
2. He, J. & Tritt, T. M. Advances in thermoelectric materials research: Looking back and moving forward. *Science* **357**, 9997 (2017).
3. Shi, X.-L., Zou, J. & Chen, Z.-G. Advanced thermoelectric design: from materials and structures to devices. *Chem. Rev.* **120**, 7399–7515 (2020).
4. Jia, N., Tan, X. Y., Xu, J., Yan, Q. & Kanatzidis, M. G. Achieving enhanced thermoelectric performance in multiphase materials. *Acc. Mater. Res.* **3**, 237–246 (2022).
5. Vineis, C. J., Shakouri, A., Majumdar, A. & Kanatzidis, M. G. Nanostructured thermoelectrics: big efficiency gains from small features. *Adv. Mater.* **22**, 3970–3980 (2010).
6. Zhao, L. D., Dravidb, V. P. & Kanatzidis, M. G. The panoscopic approach to high performance thermoelectrics. *Energ. Environ. Sci.* **7**, 251 (2014).
7. Liu, W.-D., Yang, L. & Chen, Z.-G. Cu_2Se thermoelectrics: property, methodology, and device. *Nano Today* **35**, 100938 (2020).
8. Pei, Y.-Z. et al. Stabilizing the optimal carrier concentration for high thermoelectric efficiency. *Adv. Mater.* **23**, 5674–5678 (2011).
9. Zhu, T. J. et al. Compromise and synergy in high-efficiency thermoelectric materials. *Adv. Mater.* **29**, 1605884 (2017).
10. Wang, T., Zhang, C., Snoussi, H. & Zhang, G. Machine learning approaches for thermoelectric materials research.*Adv. Funct. Mater.* **30**, 1906041 (2019).
11. Qin, D. et al. Roles of interface engineering in performance optimization of skutterudite-based thermoelectric materials. *Carbon Neutral.* **1**, 233–246 (2022).
12. Li, S. et al. In situ reaction induced core-shell structure to ultralow κ_{lat} and high thermoelectric performance of SnTe. *Adv. Sci.* **7**, 1903493 (2020).
13. Feng, D., Chen, Y.-X., Fu, L.-W., Li, J., & J.-Q. He SnSe + Ag_2Se composite engineering with ball milling for enhanced thermoelectric performance. *Rare Metals* **37**, 333–342 (2018).
14. Girard, S. N. et al. Analysis of phase separation in high performance PbTe-PbS thermoelectric materials.*Adv. Funct. Mater.* **23**, 747–757 (2013).
15. Gelbstein, Y., Davidow, J., Girard, S. N., Chung, D. Y. & Kanatzidis, M. Controlling metallurgical phase separation reactions of the $Ge_{0.87}Pb_{0.13}Te$ alloy for high thermoelectric performance. *Adv. Energy Mater.* **3**, 815–820 (2013).
16. Li, Y. et al. Enhanced thermoelectric properties of Cu_2SnSe_3 by (Ag,In)-Co-Doping.*Adv. Funct. Mater.* **26**, 6026–6032 (2016).
17. Jiang, B. et al. Realizing high-efficiency power generation in low-cost PbS-based thermoelectric materials. *Energy Environ. Sci.* **13**, 579–591 (2020).
18. Qiu, P., Xun, S. & Chen, L. Cu-based thermoelectricmaterials. *Energy StorageMater.* **3**, 85–97 (2016).
19. He Y. et al. High thermoelectric performance in non-toxic earth-abundant copper sulfide. *Adv. Mater.* **26**, 3974–3978 (2014).
20. Qiu, P., Zhu, Y., Qin, Y., Shi, X. & Chen, L. Electrical and thermal transports of binary copper sulfides Cu_xS with x from 1.8 to 1.96. *APL Mater.* **4**, 104805 (2016).
21. Zhang, Y.-X., Feng, J. & Ge, Z.-H. Enhanced thermoelectric performance of $Cu_{1.8}S$ via lattice softening. *Chem. Eng. J.* **428**, 131153 (2022).

22. Zhao, K. et al. High thermoelectric performance and low thermal conductivity in $Cu_{2-y}S_{1/3}Se_{1/3}Te_{1/3}$ liquid-like materials with nanoscale mosaic structures. *Nano Energy* **42**, 43–50 (2017).
23. Liang X., Jin D., Dai F. Phase transition engineering of Cu_2S to widen the temperature window of improved thermoelectric performance. *Adv. Electron. Mater.* **5**, 1900486 (2019).
24. Mao T. et al. Decoupling thermoelectric performance and stability in liquid-like thermoelectric materials. *Adv. Sci.* **7**, 1901598 (2019).
25. Zhang, R. et al. Optimal performance of $Cu_{1.8}S_{1-x}Te_x$ thermoelectric materials fabricated via high-pressure process at room temperature. *J. Adv. Ceram.* **9**, 535–543 (2020).
26. Tang, H. et al. Graphene network in copper sulfide leading to enhanced thermoelectric properties and thermal stability. *Nano Energy* **49**, 267–273 (2018).
27. Chen, X. et al. Carbon-encapsulated copper sulfide leading to enhanced thermoelectric properties. *ACS Appl. Mater. Inter.* **11**, 22457–22463 (2019).
28. Zhang, Z., Wu, S., Niu, Y., Jiang, J. & Wang, C. Thermoelectric properties of multi-walled carbon nanotubeembedded Cu_2S thermoelectric materials. *J. Mater. Sci. Mater. Electron.* **30**, 5177–5184 (2019).
29. Ge, Z.-H., Liu, X., Feng, D., Lin, J. & He, J. High-performance thermoelectricity in nanostructured earth-abundant copper sulfides bulk materials. *Adv. Energy Mater.* **6**, 1600607 (2016).
30. Zhao, K., Qiu, P., Shi, X. & Chen, L. Recent advances in liquid-like thermoelectric materials. *Adv. Funct. Mater.* **30**, 1903867 (2020).
31. Tang, Y.-Q. et al. Thermoelectric properties of Cu_2Se_x prepared by solution phase methods and spark plasma sintering. *J. Eur. Ceram. Soc.* **37**, 4687–4692 (2017).
32. Zhao, K. et al. Extremely low thermal conductivity and high thermoelectric performance in liquid-like $Cu_2Se_{1-x}S_x$ polymorphic materials. *J. Mater. Chem. A* **5**, 18148 (2017).
33. Mao T. et al. Enhanced thermoelectric performance and service stability of Cu_2Se via tailoring chemical compositions at multiple atomic positions. *Adv. Func. Mater.* **30**, 1908315 (2019).
34. Tang, H. et al. Enhancing the thermoelectric performance of $Cu_{1.8}S$ by Sb/Sn co-doping and incorporating multiscale defects to scatter heat-carrying phonons. *J. Mater. Chem. C.* **7**, 4026–4031 (2019).
35. Qin, P., Ge, Z.-H. & Feng, J. Effects of second phases on thermoelectric properties in copper sulfides with Sn addition. *J. Mater. Res.* **32**, 3029–3037 (2017).
36. Li, X. et al. Realizing zT>2 in environment-friendly monoclinic Cu_2S-Tetragonal $Cu_{1.96}S$ nano-phase junctions for thermoelectrics. *Angew. Chem. Int. Ed.* **61**, e202212885 (2022).
37. Meng, Q.-L. et al. Simultaneous enhancement in the power factor and thermoelectric performance of copper sulfide by In_2S_3 doping. *J. Mater. Chem. A* **4**, 12624 (2016).
38. Zhao, K. et al. Structural modularization of Cu_2Te leading to high thermoelectric performance near the mott-ioffe-regel limit. *Adv. Mater.* **34**, 2108573 (2022).
39. Zhao, K. et al. Enhanced thermoelectric performance through tuning bonding energy in $Cu_2Se_{1-x}S_x$ liquid-like materials. *Chem. Mater.* **29**, 6367–6377 (2017).
40. Qiu, P. et al. High-efficiency and stable thermoelectric module based on liquid-like materials. *Joule* **3**, 1–11 (2019).
41. Ge, Z.-H. et al. Achieving an excellent thermoelectric performance in nanostructured copper sulfide bulk via a fast doping strategy. *Mater. Today Phys.* **8**, 71–77 (2019).
42. Zhang, Y.-X. et al. Excellent thermoelectric properties and stability realized in copper sulfides based composites via complex nanostructuring. *Acta Mater.* **233**, 117972 (2022).
43. Kim, S. I. et al. Dense dislocation arrays embedded in grain boundaries for high-performance bulk thermoelectrics. *Science* **3**, 6230 (2015).
44. Carruthers, P. Scattering of phonons by elastic strain fields and the thermal resistance of dislocations. *Phys. Rev.* **114**, 995 (1959).
45. Chen, Z.-G., Shi, X., Zhao, L.-D. & Zou, J. High-performance SnSe thermoelectric materials: progress and future challenge. *Prog. Mater. Sci.* **97**, 283–346 (2018).
46. Li, M. et al. Nonperturbative quantum nature of the dislocation –phonon interaction. *Nano Lett.* **17**, 1587–1594 (2017).
47. Lukashev, P., Lambrecht, W. R. L., Kotani, T. & Schilfgaarde, M. Electronic and crystal structure of $Cu_{2-x}S$: Full-potential electronic structure calculations. *Phys. Rev. B* **76**, 195202 (2007).
48. Sun, Y.-X. et al. The "electron crystal" behavior in copper chalcogenides Cu_2X (X = Se, S). *J. Mater. Chem. A* **5**, 5098–5105 (2017).
49. Wang, H., Pei, Y., LaLonde, A. D. & Snyder, G. J. Weak electron–phonon coupling contributing to high thermoelectric performance in n-type PbSe. *Proc. Natl. Acad. Sci. USA* **109**, 9705–9709 (2012).
50. Kim, H.-S., Kang, S. D., Tang, Y., Hanus, R. & Snyder, G. J. Dislocation strain as the mechanism of phonon scattering at grain boundaries. *Mater. Horiz.* **3**, 234 (2016).
51. Cahill, D. G., Watson, S. K. & Pohl, R. O. Lower limit to the thermal conductivity of disordered crystals. *Phys. Rev. B* **46**, 6131–6140 (1992).
52. Kim, H. S., Liu, W., Chen, G., Chu, C.-W. & Ren, Z.-F. Relationship between thermoelectric figure of merit and energy conversion efficiency. *Proc. Natl. Acad. Sci. USA* **112**, 8205–8210 (2015).
53. Qiu, P. et al. Suppression of atom motion and metal deposition in mixed ionic electronic conductors. *Nat. Commun.* **9**, 2910 (2018).

Acknowledgements

We thank Dr. Lei Jin from Forschungszentrum Jülich for the help of TEM analysis. This work was supported by the Outstanding Youth Fund of Yunnan Province (Grant No. 202201AV070005), National Key R&D Program of China (No. 2022YFF0503804), Yunnan Provincial Natural Science Key Fund (Grant No. 202101AS070015), National Natural Science Foundation of China (Grant No. 52162029), Yunnan Major Scientific and Technological Projects (grant NO. 202302AG050010). All authors have given approval to the final version of the manuscript.

Author contributions

Z.H.G. and J.F. conceived the project; Y.X.Z. prepared the materials; Y.X.Z., X.Y., C.Y.W., T.Y.Y., Y.C.S. and Z.Y.W. tested TE and mechanical performance; Q.Y.H. and Q.S. performed the TEM characterization; Y.X.Z. analyzed the experimental data; Y.X.Z. wrote the manuscript. All authors participated in the data analysis and the manuscript editing.

Competing interests

The authors declare no competing interests.

Additional information

Supplementary information The online version contains supplementary material available at https://doi.org/10.1038/s41467-024-47148-0.

Correspondence and requests for materials should be addressed to Zhen-Hua Ge.

Peer review information *Nature Communications* thanks the anonymous reviewer(s) for their contribution to the peer review of this work. A peer review file is available.